DELPHI Collaboration

DELPHI 2002-025-CONF-559
19 July, 2002

Searches for invisibly decaying Higgs bosons

Marcel Stanitzki
Institut für experimentelle Kernphysik, Universität Karlsruhe
André Sopczak
Lancaster University
Guillelmo Gomez-Ceballos, Francisco Matorras
Instituto de Física de Cantabria, Universidad de Cantabria-CSIC

Abstract

Searches for HZ production with the Higgs boson decaying into an invisible final state were performed in the complete data collected by the DELPHI experiment. Both hadronic and leptonic final states of the Z boson were analysed. In addition to the search for a heavy Higgs boson, a dedicated search for a light Higgs boson with a sensitivity overlapping the mass region covered by the high-statistics LEP-1 results was performed. No signal was found. Assuming the Standard Model HZ production cross section, the mass limit for invisibly decaying Higgs bosons is 112.1 GeV/c^2. An interpretation in the Minimal Supersymmetric extension of the Standard Model (MSSM) is given.

Contributed Paper for ICHEP 2002 (Amsterdam)

1 Introduction

A search for the production of $e^+e^- \rightarrow HZ$ with $Z \rightarrow q\bar{q}$ or $Z \rightarrow \ell^+\ell^-$ and the Higgs boson decaying into stable non-interacting particles (invisible particles) was performed. The reaction is illustrated in Fig. 1. Such invisible Higgs boson decays can occur in Supersymmetry [1] or other models like Majoron models [2, 3, 4], or stable Higgs bosons which do not interact with the detector. The search described here was performed on the data collected by DELPHI in the high energy runs at 189 to 209 GeV centre-of-mass energy. These searches have been previously performed by the LEP experiments [5, 6, 7, 8].

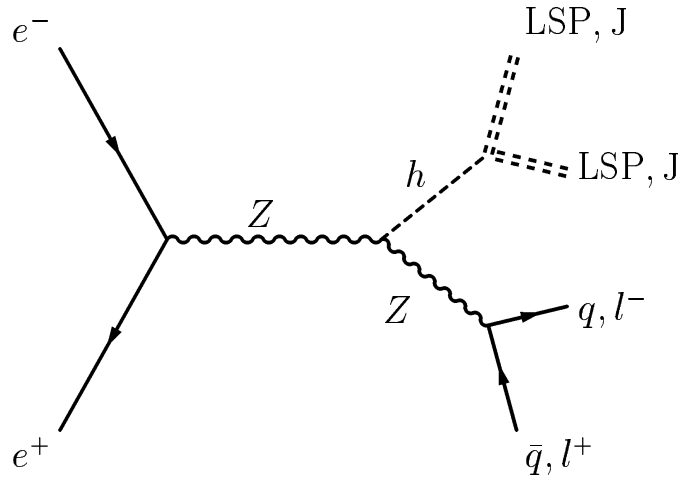

Figure 1: Feynman diagram describing the HZ production with the Higgs boson decaying into invisible particles, e.g. the lightest supersymmetric particle (LSP) or a Majoron (J) in models with an extended Higgs sector.

The event selection was mainly based on the information from the tracking system, the calorimeters, the muon chambers, and the photon veto counters of the DELPHI detector. The DELPHI detector and its performance are described in detail in Ref. [9]. The vertex detector was upgraded in recent years [10], and a set of scintillation counters were added to veto photons in blind regions of the electromagnetic calorimeter at polar angles near 40, 90 and 140 degrees. The data abalysed here were taken between the year 1998 and 2000 inclusive. For 1998 and 1999 data the centre-of-mass energies were 188.6, 191.6, 195.5, 199.5 and 201.6 GeV. For the data taken in 2000 two energies windows were defined, below and above 205.8 GeV. At the end of the year 2000 data taking, one sector of the TPC[1] was offline; this data taking period was then treated as a separate sample. This data was combined with our previous data.

2 The hadronic channel

The hadronic decay of the Z represents 70% of the HZ final states. The signature of an invisible Higgs boson decay is a pair of acoplanar and acollinear jets with a mass compatible with the Z mass and the missing energy and momentum of the invisibly

[1]Time Projection Chamber

Year	Low mass (GeV/c^2)	High mass (GeV/c^2)
1998	40-90	75-120
1999	40-100	75-120
2000	40-105	95-120

Table 1: Low and high Higgs boson mass ranges for three years of data-taking.

decaying boson. The analysed data sample corresponds to an integrated luminosity of about 592 pb^{-1} at centre-of-mass energies from 189 to 209 GeV.

The background processes $e^+e^- \to q\bar{q}(n\gamma)$ were generated using the `KK2F` generator [11]. The processes which lead to charged and neutral current four-fermion final states were generated with the `WPHACT` generator [12]. In addition, the `PYTHIA` generator [13] was used to describe the four fermion final states due to two-photon interactions. For the signal simulation the `HZHA` generator [14] was used.

For all the years of data-taking the following simulated signal samples were generated:

- 40 to 90 GeV/c^2 in 5 GeV/c^2, 90 to 115.0 GeV/c^2 in 2.5 GeV/c^2 steps and 120 GeV/c^2 .

Both signal and background events were processed through the full DELPHI detector simulation [9].

In order to obtain a good performance in the whole mass range, two mass windows were defined and the analyses were optimised for each window as defined in Table 1.

2.1 High mass analysis

The selection of HZ candidate events consists of several steps aimed at rejecting the data taken when the detector was not fully operational, and on suppressing $\gamma\gamma$ and radiative returns to the on-shell Z background. Then an Iterative Discriminant Analysis (IDA) [15] was applied to select candidates.

- Detector quality veto: A detector quality selection was used, requiring that both the tracking system and the calorimeters be fully operational.

- Anti-$\gamma\gamma$: This selection suppresses most of the $\gamma\gamma$ background. Each event was required to have at least 9 charged tracks, 2 charged tracks with transverse momentum greater than 2 GeV/c and impact parameters less than 1 mm in the transverse plane and less than 3 mm along the beam axis. The charged energy is required to be greater than $0.16\sqrt{s}$, no electromagnetic shower with more than $0.45\sqrt{s}$, the transverse energy greater than $0.15\sqrt{s}$ and the sum of the longitudinal momenta greater than $0.25\sqrt{s}$.

- Anti-radiative return and anti-WW: This selection was applied to suppress most of the background events resulting from radiative return to the Z-pole. It contained a two-dimensional cut in the $\theta_{\mathrm{p_{mis}}}$ vs. E' plane, requiring

  $40^\circ \leq \theta_{\mathrm{p_{mis}}} \leq 140^\circ$ and $E' \geq 115$ GeV,

where E′ stands for the effective centre-of-mass energy after the emission of one or more photons and $\theta_{\mathrm{p_{mis}}}$ is polar angle of the missing momentum. Other requirements were that less than $0.08\sqrt{s}$ was deposited in the STIC[2] [9], $\mathrm{E}'/\sqrt{\mathrm{s}}$ was less 0.96 and that the total electromagnetic energy below 30° was less than $0.16\sqrt{s}$. In order to suppress badly reconstructed events, candidates in which a jet pointed to cracks between barrel and endcap detectors or where both jets were below 12° are rejected. A hermeticity veto algorithm was applied to ensure that no photon has escaped in the blind region of the electromagnetic calorimeter at polar angles near 40, 90 and 140 degrees. The energy of the leading particle was required to be less than $0.2\sqrt{s}$ and the transverse momentum with respect to the jet (forcing the event into a two-jet configuration) to be less than $0.05\sqrt{s}$. Finally, we required that upon forcing the event into a three-jet configuration, every jet had at least one charged track.

Twelve variables were used to construct a performant tagging variable in the framework of the IDA. In order to calculate these variables, the event was forced into 2 jets, using the DURHAM [16] algorithm.

- $E_\gamma/E_\gamma^{\mathrm{Z}}$: the normalised energy of a photon assumed to have escaped in the beam direction, deduced from the polar angles of the two main jet directions in the event. The photon energy was normalised to the energy expected for a photon recoiling against an on-shell Z.
- $\ln(p_{\mathrm{T}})$: logarithm of the transverse momentum of the event.
- $E_{\mathrm{vis}}/\sqrt{s}$: visible energy of the event, normalised to the centre-of-mass energy.
- $E_{\mathrm{T}}/\sqrt{s}$: transverse energy of the event, normalised to the centre-of-mass energy.
- θ_{cone}: polar angle containing 6% of the visible energy.
- $\cos(\theta_{\vec{p}_{\mathrm{mis}}})$: cosine of the missing momentum angle to the z-axis.
- E_{isol}: energy sum in the double cone, defined by half opening angles 5° and α_{max} around the most isolated particle. The most isolated particle is defined as the particle with momentum above 2 GeV/c with the smallest energy sum in the double cone. In the momentum interval from 2 to 5 GeV/c, α_{max} is set to 60° in order to maximise the sensitivity to isolated particles from tau decays in $\mathrm{WW} \to \mathrm{q\bar{q}}'\tau\nu$ events, while an opening angle of 25° is used for particles with higher momenta.
- $p_{\mathrm{isol}}/\sqrt{s}$: momentum of the most isolated particle, as defined above.
- log(acoplanarity): $\log_{10}$ of the acoplanarity. The acoplanarity is defined as $180° - \Delta\phi$, where $\Delta\phi$ is the difference in azimuthal angle (in the plane perpendicular to the beam axis) between the two jets, when forcing the reconstruction in exactly two jets. In order to compensate for the geometrical instability of this variable for jets at low angles it was scaled with the angle between the 2 jets.
- Thrust: thrust value of the event, computed in the rest frame of the visible system. The transformation into the rest frame is made in order to compensate the smearing due to the boost of the jet system.

[2]Small angle TIle Calorimeter, covering the very forward region.

Variable	lower cut	upper cut
E_γ/E_γ^Z	0.0	0.90
$\ln(p_T)$	1.75	4.5
$E_T/\sqrt{s}$	0.15	0.6
$\cos(\vec{p}_{mis})$	0.0	1.0
$p_{isol}/\sqrt{s}$	0.008	0.18
log(acoplanarity)	0.3	2.5
Thrust	0.65	1.0
ln(acollinearity)	2.0	4.5
$\ln(\max(p_T)_{jet})$	-0.5	2.50

Table 2: Tail cuts used in the high mass hadronic analysis. The variables are described in detail in sec. 2.1.

- ln(acollinearity): logarithm of the acollinearity of the two-jet system.
- $\ln(\max(p_T)_{jet})$: highest transverse momentum of the jet-particles, defined by the transverse momentum of any particle in the jet with respect to the nearest jet axis.

The cuts listed in Table 2 were applied in the tails of these variable distributions in order to concentrate on the signal region. In addition, the signal was further enriched by requiring that the number of identified leptons in an event be less than three. The simulation agrees well with the data as shown in Table 3 and Fig. 2.

$\sqrt{s}$	Anti-$\gamma\gamma$		Anti-radiative returns		Tail cuts	
(GeV)	Data	MC	Data	MC	Data	MC
188.6	15115	14967.0 ± 8.1	1578	1565.2 ± 6.0	494	485.9 ± 3.2
191.6	2394	2351.8 ± 1.3	258	249.9 ± 0.9	88	79.0 ± 0.5
195.5	7040	6531.3 ± 3.5	739	715.5 ± 2.5	242	237.6 ± 1.4
199.5	7296	7168.9 ± 3.9	784	795.4 ± 2.8	295	264.4 ± 1.6
201.6	3557	3407.8 ± 1.9	396	382.9 ± 1.3	152	130.6 ± 0.7
205.0	6272	6018.8 ± 3.8	678	686.5 ± 2.4	240	239.3 ± 1.4
206.5	6772	6722.6 ± 8.0	798	774.0 ± 4.0	283	267.7 ± 1.6
206.5U	4472	4560.4 ± 3.9	534	541.5 ± 2.6	202	190.7 ± 1.5

Table 3: Comparison of simulation and data after the different steps of the preselection in the high-mass hadronic analysis. The listed errors are from Monte Carlo statistics only.

Two IDA steps were performed in order to obtain optimal signal to background discrimination. The background versus efficiency curve for one centre-of-mass energy is shown in Fig. 3. The working point was determined by maximising the expected mass limit as a function of efficiency. The final selection is indicated by the vertical line. It is indicated by the dashed line in Fig. 3. This working point was obtained separately for each centre-of-mass energy, optimising the analysis for a 85 GeV/c^2 Higgs boson at 188.6 GeV, for a 95 GeV/c^2 Higgs boson at 191.6 and 195.6 GeV, for a 100 GeV/c^2 Higgs at 199.5 and 201.6 GeV and for a 105 GeV/c^2 Higgs for 205.0 and 206.5 GeV.

Variable	lower cut	upper cut
E_γ/E_γ^Z	0.0	1.20
$E_\mathrm{T}/\sqrt{s}$	0.0	0.6
$p_\mathrm{isol}/\sqrt{s}$	0.0	0.18
log(acoplanarity)	1.0	2.5
ln(acollinearity)	2.25	4.5

Table 4: Tail cuts used in the low mass hadronic analysis. The variables are described in detail in sec. 2.1.

2.2 Low-mass analysis

For the low-mass analysis, the preselection was adapted due to different event shape and kinematics. In the anti-radiative return selection the two-dimensional cut in the $\theta_{\mathrm{p_{mis}}}$ vs. E′ plane, requiring

$$40^\circ \leq \theta_{\mathrm{p_{mis}}} \leq 140^\circ \text{ and } \mathrm{E}' \geq 115 \text{ GeV},$$

and the cut requiring $\mathrm{E}'/\sqrt{\mathrm{s}}$ to be less than 0.96 were removed in order to increase the signal efficiency. Some tail cuts were also slightly adapted as shown in Table 4 and a cut requiring the visible mass to be at least 20% of $\sqrt{s}$ was added. Figure 5 shows the agreement of data and background at the preselection level.

$\sqrt{\mathrm{s}}$	Anti-$\gamma\gamma$		Anti-radiative returns		Tail cuts	
(GeV)	Data	MC	Data	MC	Data	MC
188.6	15115	14967.0 ± 8.1	6604	6735.2 ± 11.0	622	652.0 ± 3.9
191.6	2394	2351.8 ± 1.3	1013	1051.2 ± 1.7	112	103.0 ± 0.6
195.5	7040	6531.3 ± 3.5	2939	2876.8 ± 4.6	322	294.0 ± 1.6
199.5	7296	7168.9 ± 3.9	3122	3117.7 ± 5.0	338	315.1 ± 1.8
201.6	3557	3407.8 ± 1.9	1551	1495.9 ± 2.4	168	152.1 ± 0.8
205.0	6272	6018.8 ± 3.8	2617	2616.7 ± 4.4	344	307.9 ± 1.6
206.5	6772	6722.6 ± 8.0	2885	2922.4 ± 6.6	305	293.6 ± 1.7
206.5U	4472	4560.4 ± 3.9	1878	1982.5 ± 4.7	257	237.5 ± 1.7

Table 5: Comparison of simulation and data after the different steps of the preselection in the low-mass hadronic analysis. The errors given are from Monte Carlo statistics only. The last lines of each channel (206.5U) refers to the data taken with one TPC sector inoperative, which has been fully taken into account in the event simulations.

The low mass analysis also used IDA steps in order to obtain optimal signal to background discrimination. The background versus efficiency curve for one centre-of-mass energy is shown in Fig. 6. The working point was obtained separately for each centre-of-mass energy as described above. It was optimised for a 60 GeV/c^2 Higgs boson mass at all energies.

2.3 Mass reconstruction

The recoil mass to the di-jet system, which corresponds to the mass of the invisible Higgs boson, was calculated with a Z-mass constraint for the measured di-jet system, from the visible energy and the visible mass, using the following expression

$$m_{\mathrm{inv}} = \sqrt{\left(\sqrt{\mathrm{s}} - \frac{m_{\mathrm{Z}} E_{\mathrm{vis}}}{m_{\mathrm{vis}}}\right)^2 - \left(\frac{m_{\mathrm{Z}} p_{\mathrm{mis}}}{m_{\mathrm{vis}}}\right)^2},$$

where p_{mis} is the missing momentum and m_{Z} is the Z mass ($c \equiv 1$). The recoil mass distribution after the final selection for the high-mass analysis is shown in Fig. 4. For the low-mass region this method was also used, but in cases where one obtained masses around 1 GeV the standard missing calculation $\sqrt{E_{\mathrm{mis}}^2 - p_{\mathrm{mis}}^2}$was used. The recoil mass distribution for the low mass region is shown in Fig. 7.

2.4 Systematic errors

The effect of modelling QCD fragmentation in the $\mathrm{q\bar{q}}(n\gamma)$ background was studied by replacing the `KK2F` generator with the `ARIADNE` generator [17] at 206.5 GeV. The results were identical within statistical errors. The error of the luminosity is assumed to be 0.5%. The process $\mathrm{e^+e^-} \to \mathrm{q\bar{q}e\bar{\nu}}$ provides about a fifth of the background and the uncertainty on the cross section of this process is assumed to be 5% [18]. This attributes to about 1% of the background uncertainty. In order to see the influence of the jet clustering algorithm the DURHAM algorithm was replaced by the LUCLUS algorithm [19]. This is an indication of possible uncertainty on the background estimation and the signal efficiency in the order of 1% for the high mass regime and an error in the order of 2.5% for the low mass regime.

In order to estimate the effect of Monte Carlo imperfections in describing LEP2 data a so-called shaking procedure was used, as first applied in the $\mathrm{ZZ} \to \mathrm{q\bar{q}}\nu\bar{\nu}$ analysis [20]. First the data and Monte-Carlo agreement of $\mathrm{Z} \to \mathrm{q\bar{q}}$ events taken at $\sqrt{s} = 91.1$ GeV for the corresponding year of data taking was studied for the charged and neutral multiplicities of the events. The events multiplicities were studied separately for the barrel ($\cos\theta \leq 0.7$) and the forward region ($\cos\theta > 0.7$) and for different momentum bins. For each of these classes of multiplicities a separate correction factor P was calculated using

$$P = \frac{< N_{\mathrm{data}} > - < N_{\mathrm{MC}} >}{< N_{\mathrm{MC}} >}$$

The correction factors are larger for neutral tracks than for charged tracks and also larger in the forward region. The correction factors obtained were then applied to the LEP2 Monte Carlo simulation on an event per event basis. The factor P was used as a probability whether to add or remove tracks in the Monte Carlo simulation. If P was less than zero, there were fewer tracks in data than in Monte Carlo and the tracks of the corresponding class were removed in the simulated events. For P greater than zero, tracks have to be added to the simulated events. This was performed using another track of the same class and smearing its momentum by 2.5%. If there was no track of the corresponding class, a track of the neighbouring class was taken and scaled to fit into this class.

The analysis was then applied on theses samples, the differences obtained were used as an estimate of the systematic error. The effect on the background estimation ranges from

10.5% (1998), 4.7% (1999) to 10.6%(2000) for the high mass regime. For the low mass regime the effects are smaller, they range from 6.6 % (1998), 4.3% (1999) to 5.6% (2000). The shaking also affects the signal efficiencies leading to a reduction of the relative signal efficiency of up to 1.5%. Details of the systematic error, combined with the errors from MC statistics are shown in Table 7 and Table 8.

3 Leptonic channels

The leptonic channel $H\ell^+\ell^-$ represents about 10% of the HZ final state. The experimental signature of the HZ($Z \to \ell^+\ell^-$) final states is a pair of acoplanar and acollinear leptons, with an invariant mass compatible with the expectation from $Z \to \ell^+\ell^-$. The signal and the background simulations were performed with the same programs as the hadronic channel, except that the `KORALZ` generator [21] was used for $\tau^+\tau^-(n\gamma)$ events, the `KK2F` generator [11] for $\mu^+\mu^-(n\gamma)$ events and the `BHWIDE` generator [22] for the Bhabha processes. The leptonic two-photon processes were generated with `BDK` generator [23]. The relevant backgrounds arise from four fermion processes, di-leptons from $e^+e^- \to Z(\gamma) \to e^+e^-$, Bhabha scattering and two-photon collisions.

The analysis contains a preselection for leptonic events. Then, the search channel is defined by the lepton-type of the Z decay mode and for each decay mode specific selection cuts were applied. Two separated analyses were used depending on the reconstructed mass, defining the low-mass and high-mass analyses.

3.1 Leptonic preselection

An initial set of cuts was applied to select a sample enriched in leptonic events. A total charged particle multiplicity between 2 and 6 was required. All particles in the event were clustered into jets using the LUCLUS algorithm [19] ($d_{\rm join} = 6.5$ GeV/c) and only events with two reconstructed jets were retained. Both jets had to contain at least one charged particle and at least one jet had to contain exactly one charged particle.

In order to reduce the background from two-photon collisions and radiative di-lepton events, the event acoplanarity, $\theta_{\rm acop}$, the acollinearity of the two jet directions projected onto the plane perpendicular to the beam axis, had to be larger than 2 degrees, and the acollinearity, $\theta_{\rm acol}$, had to be larger than 3 degrees. In addition, the total momentum transverse to the beam direction, P_t, had to exceed $0.02\sqrt{s}$. Finally, the energy of the most energetic photon was required to be less than $0.15\sqrt{s}$, and the angle between that photon and the charged system projected onto the plane perpendicular to the beam axis had to be less than 170 degrees. The number of data and simulated background events are given in Table 6 for each center-of-mass energy.

3.2 Channel identification

For the preselected events, jets were then identified as either μ, e or τ and two leptons with the same flavour were required. A particle was identified as a muon if at least one hit in the muon chambers was associated to it, or if it had energy deposited in the outermost layer of the hadron calorimeter. In addition, the energy deposited in the other layers had to be compatible with that from a minimum ionising particle. For the identification of

$\sqrt{s}$	$\mu^+\mu^-$		e^+e^-		$\tau^+\tau^-$	
(GeV)	Data	MC	Data	MC	Data	MC
188.6	64	49.7 ± 0.8	314	298.0 ± 7.1	124	148.2 ± 3.7
191.6	10	7.9 ± 0.1	46	45.5 ± 1.1	18	22.4 ± 0.8
195.5	19	22.5 ± 0.3	132	125.5 ± 3.1	78	62.2 ± 2.1
199.5	24	24.8 ± 0.3	149	134.6 ± 3.2	81	74.9 ± 1.8
201.6	17	12.1 ± 0.2	60	65.9 ± 1.6	34	32.1 ± 1.1
205.0	11	20.5 ± 0.3	98	114.2 ± 2.7	70	55.3 ± 1.0
206.5	26	23.1 ± 0.3	110	129.5 ± 2.2	76	71.9 ± 1.1
206.5U	6	14.6 ± 0.2	79	76.3 ± 1.9	48	40.3 ± 1.3

Table 6: Comparison of simulation and data at preselection level in the three leptonic channels. The errors reflect the Monte Carlo statistics only. The last lines of each channel (206.5U) refers to the data taken with one TPC sector inoperative, which has been fully taken into account in the event simulations.

a particle as an electron the energies deposited in the electromagnetic calorimeters, in the different layers of the hadron calorimeter, and in addition the energy loss in the time projection chamber were used. A lepton was identified as a cascade decay coming from a τ if the momentum was lower than $0.13\sqrt{s}$.

3.3 Channel dependent criteria

After the preselection, different cuts were applied in each channel in order to reduce the remaining background. There is no overlap of the event samples in the channels. The optimisation of the efficiency has been performed for mass ranges of 50 to 85 GeV/c^2 and 85 to 115 GeV/c^2.

In the $\mu^+\mu^-$ channel the direction of the missing momentum had to deviate from the beam axis by more that 18° in order to reject $Z \to \mu^+\mu^-(\gamma)$ and $\gamma\gamma \to \mu^+\mu^-$ processes; and the di-muon mass was required to be between 75 GeV/c^2 and 97.5 GeV/c^2, to be consistent with the Z boson mass. After that, two different cut ranges were applied depending on the reconstructed mass. If the reconstructed mass was higher than 85 GeV/c^2 the momentum of the most energetic muon had to be between $0.2\sqrt{s}$ and $0.4\sqrt{s}$, the visible energy, $E_{\rm vis}$, less than $0.55\sqrt{s}$, $P_t < 0.25\sqrt{s}$ and $\theta_{\rm acol} < 60°$. Otherwise, the momentum of the most energetic muon had to be between $0.25\sqrt{s}$ and $0.45\sqrt{s}$, $0.45\sqrt{s} < E_{\rm vis} < 0.65\sqrt{s}$, $P_t < 0.4\sqrt{s}$ and $45° < \theta_{\rm acol} < 85°$.

In the e^+e^- channel, the most important background arises from radiative Bhabha scattering and Ze^+e^- events. To suppress these backgrounds, the direction of the missing momentum and the polar angle of both leptons had to deviate from the beam axis by more than 18°, the transverse energy had to be greater than $0.15\sqrt{s}$ and the neutral electromagnetic energy less than $0.1\sqrt{s}$. The invariant mass of both leptons has to be between 75 GeV/c^2 and 100 GeV/c^2, to be consistent with the Z boson mass. Then, if the mass reconstructed was higher than 85 GeV/c^2: the momentum of the most energetic electron had to be lower than $0.35\sqrt{s}$, the total associated energy was required to be less than $0.55\sqrt{s}$, $P_t < 0.25\sqrt{s}$ and $\theta_{\rm acol} < 60°$. Otherwise, the momentum of the most energetic electron had to be between $0.25\sqrt{s}$ and $0.45\sqrt{s}$, the total associated energy was

required to be less than $0.65\sqrt{s}$, $P_t < 0.4\sqrt{s}$ and $45^\circ < \theta_{\rm acol} < 85^\circ$.

In the $\tau^+\tau^-$ channel tighter cuts were applied on the acoplanarity and acollinearity in order to reduce remaining background from $\tau^+\tau^-(\gamma)$ and $\gamma\gamma \to \ell\ell$ processes. The invariant mass of both jets had to be less than 3 GeV/c^2. In addition the transverse energy had to be greater than $0.1\sqrt{s}$ the visible energy of all particles with $|\cos\theta| < 0.9$ had to be greater than $0.06\sqrt{s}$ and the energy of both jets had to be less than $0.26\sqrt{s}$. Finally, if the mass reconstructed was higher than 85 GeV/c^2, the acollinearity had to be between 10 and 60 degrees, and between 45 and 85 degrees in the other case.

3.4 Systematic uncertainties

Several sources of systematic uncertainties were investigated for their effect on the signal efficiency and the background rate. The particle identification was checked with di-leptons samples both at Z peak and high energy, and the simulated and data rate agrees within 1%. The modelling of the preselection variables agrees within statistical errors with the data. The track selection and the track reconstruction efficiency was also taken into account in the total systematic error. The effects of detector miss-calibration and deficiencies were investigated using events compatible with $\mu^+\mu^-\gamma$ or $e^+e^-\gamma$ processes. The comparison between data and simulation rate was found to be better than 1%. Additional systematic effects were estimated by comparing the data collected at Z peak during the period with TPC[3]-sector-6 off with simulation samples produced with the same detectors conditions. The total systematic error on the signal efficiency was 1.1%. The total systematic error on the background rate was up to 10%. The total systematic error and statistical error from the limited MC statistics are combined and given in Table. 7.

3.5 Mass reconstruction

The mass of the invisibly decaying particle was computed from the measured energies assuming momentum and energy conservation. To improve the resolution a χ^2 fit was applied constraining the visible mass to be compatible with a Z. In the case of the $\tau^+\tau^-$ channel, the information carried by the decay products does not reproduce correctly the τ energy. Therefore, the mass was calculated under the assumption that both τ leptons had the same energy. This, together with the visible mass constraint, allowed an estimation of this energy and of the invisible mass. The invisible mass for the candidates as well as for the expected background from Standard Model processes for the different channels is shown in Fig. 8.

4 Results

A comparison of observed and predicted numbers of selected events for the four channels are summarised in Table 7. The agreement between data and background is good for all channels and no indication of an invisible Higgs boson signal has been observed.

[3]Time Projection Chamber

$\sqrt{s}$ (GeV)	Channel	Luminosity pb^{-1}	Data	Expected background	Signal efficiency %
189	$q\bar{q}$	152.4	65	71.3 ± 7.7	40.9 ± 1.9
192	$q\bar{q}$	24.7	2	5.6 ± 0.3	39.6 ± 1.7
196	$q\bar{q}$	74.3	21	18.5 ± 1.0	50.8 ± 1.7
200	$q\bar{q}$	82.2	21	20.1 ± 1.0	51.9 ± 1.7
202	$q\bar{q}$	40.0	11	10.8 ± 0.5	50.7 ± 1.7
205	$q\bar{q}$	74.3	9	12.2 ± 1.3	36.4 ± 2.1
206.5	$q\bar{q}$	82.8	13	13.5 ± 1.5	37.0 ± 2.1
206.5U	$q\bar{q}$	58.0	11	8.4 ± 0.9	31.6 ± 2.1
189	$\mu^+\mu^-$	153.8	7	6.9 ± 0.6	44.0 ± 1.9
192	$\mu^+\mu^-$	24.5	4	1.1 ± 0.1	52.8 ± 1.6
196	$\mu^+\mu^-$	72.4	3	3.5 ± 0.2	63.8 ± 1.5
200	$\mu^+\mu^-$	81.8	0	3.9 ± 0.3	63.0 ± 1.5
202	$\mu^+\mu^-$	39.4	2	1.8 ± 0.2	62.5 ± 1.5
205	$\mu^+\mu^-$	69.1	0	3.0 ± 0.3	62.8 ± 1.5
206.5	$\mu^+\mu^-$	79.8	2	3.3 ± 0.3	62.1 ± 1.5
206.5U	$\mu^+\mu^-$	50.0	0	2.2 ± 0.2	56.9 ± 1.6
189	e^+e^-	153.8	4	7.9 ± 0.7	34.2 ± 1.3
192	e^+e^-	24.5	1	1.2 ± 0.2	40.8 ± 1.6
196	e^+e^-	72.4	4	4.7 ± 0.5	45.3 ± 1.6
200	e^+e^-	81.8	5	4.1 ± 0.4	45.2 ± 1.6
202	e^+e^-	39.4	1	1.9 ± 0.2	45.1 ± 1.6
205	e^+e^-	69.1	3	3.6 ± 0.3	44.8 ± 1.6
206.5	e^+e^-	79.8	1	4.0 ± 0.4	42.9 ± 1.6
206.5U	e^+e^-	50.0	1	2.3 ± 0.3	39.9 ± 1.6
189	$\tau^+\tau^-$	153.8	7	9.4 ± 0.8	21.4 ± 1.4
192	$\tau^+\tau^-$	24.5	1	1.9 ± 0.2	17.3 ± 1.4
196	$\tau^+\tau^-$	72.4	7	5.7 ± 0.6	20.2 ± 2.1
200	$\tau^+\tau^-$	81.8	10	6.3 ± 0.6	27.3 ± 1.5
202	$\tau^+\tau^-$	39.4	2	3.3 ± 0.4	28.2 ± 1.5
205	$\tau^+\tau^-$	69.1	5	5.7 ± 0.6	29.5 ± 1.5
206.5	$\tau^+\tau^-$	79.8	3	7.1 ± 0.7	30.3 ± 1.5
206.5U	$\tau^+\tau^-$	50.0	2	4.5 ± 0.4	29.5 ± 1.5

Table 7: Integrated luminosity, observed number of events, expected number of background events and signal efficiency (100 GeV/c^2 signal mass) for different energies. The last lines of each channel (206.5U) refers to the data taken with one TPC sector inoperative, which has been fully taken into account in the event simulations.

$\sqrt{s}$ (GeV)	Channel	Luminosity pb^{-1}	Data	Expected Background	Signal efficiency (%)
189	$q\bar{q}$	152.8	58	51.5 ± 3.8	49.1 ± 1.6
192	$q\bar{q}$	24.9	6	10.1 ± 0.5	50.0 ± 1.7
196	$q\bar{q}$	75.0	36	31.4 ± 1.6	49.6 ± 1.7
200	$q\bar{q}$	82.2	37	44.3 ± 2.3	50.5 ± 1.7
202	$q\bar{q}$	40.4	10	12.0 ± 0.6	44.2 ± 1.7
205	$q\bar{q}$	76.3	26	26.2 ± 1.7	47.0 ± 1.5
206.5	$q\bar{q}$	82.8	30	33.4 ± 2.1	48.8 ± 1.5
206.5U	$q\bar{q}$	58.0	10	18.0 ± 1.2	43.6 ± 1.5

Table 8: Integrated luminosity, observed number of events, expected number of background events and signal efficiency (60 GeV/c^2 signal mass) for different energies in the low mass analysis. The last lines of each channel (206.5U) refers to the data taken with one TPC sector inoperative, which has been fully taken into account in the event simulations.

4.1 Model independent limits

The cross-section and mass limits were computed with a likelihood method [24]. All search channels and centre-of-mass energies were treated as separate experiments to obtain a likelihood function. In total 40 channels, as listed in Table 7, the $q\bar{q}$ channels from 161 and 172 GeV data [5], and the $q\bar{q}$ and $\mu^+\mu^-$ channels from 183 GeV data [6] were evaluated. In order to adress the overlap between the low and high mass analyses in the hadronic channel, the expected performance was calculated for both analyses in the overlap region. The analysis being more performant at a given mass, was then chosen for the limit calculation.

Figure 10 displays the observed and expected upper limits on the cross-section for the process $e^+e^- \rightarrow Z(\text{anything})H(\text{invisible})$ as a function of the Higgs boson mass. From the comparison with the Standard Model (SM) Higgs boson cross-section the observed (expected) mass limits are 112.1 (110.5) GeV/c^2 for the Higgs boson decaying into invisible particles.

4.2 Limits for a Majoron model

The limits computed above can be used to set a limit on the Higgs bosons in a Majoron model [2, 3, 4] with one doublet ϕ and one singlet η. Mixing of the real parts of ϕ and η leads to two massive Higgs bosons:

$$H = \phi_R \cos\theta - \eta_R \sin\theta$$

$$S = \phi_R \sin\theta + \eta_R \cos\theta$$

where θ is the mixing angle. The imaginary part of the singlet is identified as the Majoron. The Majoron is decoupled from the fermions and gauge bosons, but might have a large coupling to the Higgs bosons. In this model the free parameters are the masses of H and S, the mixing angle θ and the ratio of the vacuum expectation values of the two fields ϕ and η ($\tan\beta \equiv \frac{v_\phi}{v_\eta}$). The production rates of the H and S are reduced with respect to the SM Higgs boson, by factors of $\cos^2\theta$ and $\sin^2\theta$, respectively. The decay widths of the H

and S into the heaviest possible fermion-antifermion pair are reduced by the same factor and their decay widths into a Majoron pair are proportional to the complementary factors ($\cos^2\theta$ for S and $\sin^2\theta$ for H). In the case where the invisible Higgs boson decay mode is dominant ($\tan\beta$ large), the excluded region in the mixing angle versus Higgs boson mass plane is shown in Fig. 11.

4.3 Limits in the MSSM

Parameter regions in the MSSM are identified where the Higgs boson can decay into neutralinos $\tilde{\chi}^0$, which leads to invisible Higgs decays. The m_h − max scenario benchmark parameters [27] were modified to obtain light neutralino masses setting $M_2 = \mu =$ 150 GeV/c^{2}and the other parameters remain unchanged. Then, a scan was performed in the $\tan\beta$-m_A plane. For each scan point the hZ production cross section and the Higgs boson branching ratio into neutralinos were calculated. If the cross section for a Higgs boson decaying into neutralinos was then larger than excluded cross section as shown in Fig. 10, this point was excluded. Figure 12 shows the following regions: a) excluded from the search for invisible Higgs decays, b) theoretically forbidden, and c) the branching ratio $h \to \tilde{\chi}^0\tilde{\chi}^0$ is less than 1%. For the m_h-max scenario, the invisible Higgs boson search covers a large region in the low $\tan\beta$ regime. Most of the unexcluded parameter regions (white area) are excluded when in addition the search channels for the visible Higgs boson decays are considered in the framework of a general MSSM parameter scan [28].

5 Conclusion

In the complete data samples collected by the DELPHI detector at a centre-of-mass energy of 188.6 to 209.0 GeV, 153 $q\bar{q}$, 18 $\mu^+\mu^-$, 20 e^+e^- and 37 $\tau^+\tau^-$ events were selected in searches for a Higgs boson decaying into invisible final states. These numbers are consistent with the expectation from SM background processes.

We set a 95% CL lower mass limit of 112.1 GeV/c^2 for Higgs bosons with a Standard Model cross-section and with 100% branching fraction into invisible decays. The invisible Higgs boson search is important to cover some parameter regions in the MSSM, where Higgs decays into neutralinos are kinematically allowed.

References

[1] A. Djouadi, P. Janot, J. Kalinowski and P.M. Zerwas, *Phys. Lett.* **B376** (1996) 220.

[2] Y. Chikashige, R.N. Mohapatra, R.D. Peccei,*Phys. Lett.* **B98** (1981) 265;
R.E. Shrock, M. Suzuki, *Phys. Lett.* **B110** (1982) 250;
R. Mohapatra, J.W.F. Valle, *Phys. Rev.* **D34** (1986) 1642;
M.C. Gonzalez-Garcia, J.W.F. Valle, *Phys. Lett.* **B216** (1989) 360;
E.D Carlson, L.J. Hall, *Phys. Rev.* **D40** (1989) 3187;
L.F. Li,Y. Liu, L. Wolfenstein, *Phys. Lett.* **B159** (1985) 45;
A. Zee, *Phys. Lett.* **B93** (1980) 389.

[3] F. de Campos et al.,*Phys. Rev.* **D55** (1997) 1316.

[4] S.P. Martin and J.D. Wells,*Phys. Rev.* **D60** (1999) 035006.

[5] DELPHI Collaboration, P. Abreu et al., *Eur. Phys. J.* **C2** (1998) 1.

[6] DELPHI Collaboration, P. Abreu et al., *Phys. Lett.* **B459** (1999) 367.

[7] ALEPH Collaboration, A. Heister *et al.* Phys. Lett. B **526** (2002) 191.

[8] L3 Collaboration, M. Acciarri *et al.*, Phys. Lett. B **485** (2000) 85.

[9] DELPHI Collaboration, P. Abreu et al., *Nucl. Instr. and Meth.* **378** (1996) 57;
DELPHI Collaboration, P. Aarnio et al, *Nucl. Instr. and Meth.* **A303** (1991) 233.

[10] DELPHI Silicon Tracker Group,P. Chochula et al., *Nucl. Instr. and Meth.* **A412** (1998) 304.

[11] S. Jadach, B. F. Ward and Z. Was, *Comp. Phys. Comm.* **130** (2000) 260.

[12] E. Accomando and A. Ballestrero, *Comp. Phys. Comm.* **99** (1997) 270.

[13] T. Sjöstrand, *Comp. Phys. Comm.* **39** (1986) 347;
Comp. Phys. Comm. **82** (1994) 74.

[14] P. Janot, in CERN Report 96-01, Vol. 2, p. 309.

[15] T.G.M. Malmgren, *Comp. Phys. Comm.* **106** (1997) 230;
T.G.M. Malmgren and K.E. Johansson, *Nucl. Instr. and Meth.* **403** (1998) 481.

[16] S. Catani, Y. L. Dokshitzer, M. Olsson, G. Turnock and B. R. Webber, *Phys. Lett.* **BB269** (1991) 432.

[17] L. Lonnblad, *Comp. Phys. Comm.* **71** (1992) 15.

[18] M. W. Grunewald et al., In CERN Report 2000-009 p 1-135. *Four-fermion production in electron positron collisions.*

[19] T. Sjöstrand, *PYTHIA 5.7 / JETSET 7.4*, CERN-TH.7112/93 (1993).

[20] DELPHI Collaboration, P. Abreu et al., *ZZ production in e+e- interactions at $\sqrt{s}$=183-209 GeV*, to be published.

[21] S. Jadach, W. Placzek and B. F. Ward, *Phys. Lett.* **B390** (1997) 298.

[22] S. Jadach, B. F. Ward and Z. Was, *Comp. Phys. Comm.* **79** (1994) 503.

[23] F.A. Berends, P.H. Daverveldt, R. Kleiss, *Nucl. Phys.* **B253** (1985) 421; *Comp. Phys. Comm.* **40** (1986) 271,285 and 309.

[24] A.L. Read, in CERN Report 2000-005 p. 81 (2000).

[25] DELPHI Collaboration, P. Abreu et al., *Eur. Phys. J.* **C17** (2000) 187.

[26] DELPHI Collaboration, P. Abreu et al., **EP 2001-087** (in press) *Eur.Phys.J* **C**.

[27] DELPHI Collaboration, P. Abreu et al., *MSSM Higgs searches*, contribution to ICHEP, Amsterdam, August 2002.

[28] A. Sopczak, Proceedings of the Seventh Topical Seminar on the Legacy of LEP and SLC, Siena, Italy, October 2001, in press *Nucl.Phys.*, hep-ph/0112086.

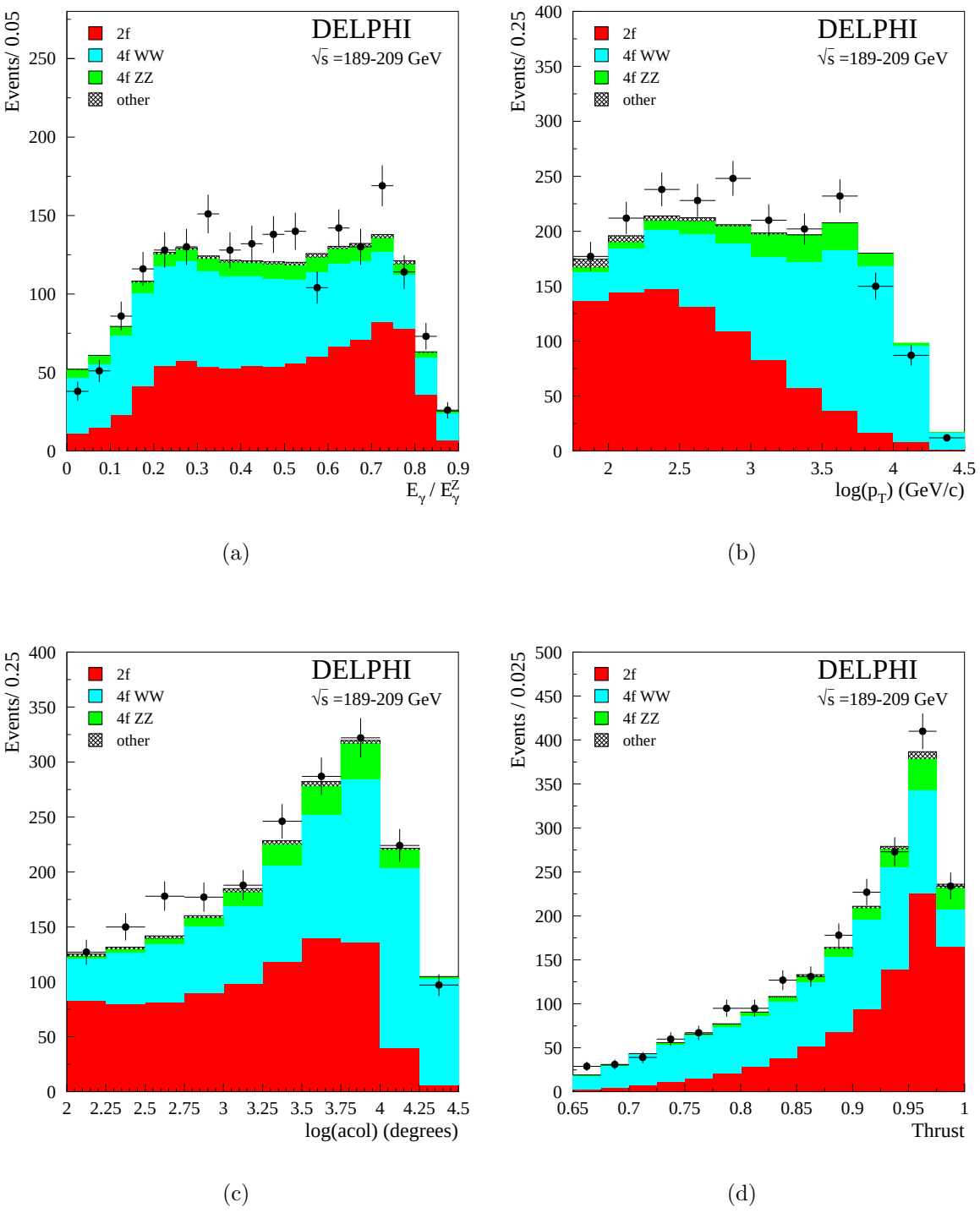

Figure 2: Distributions for the preselection variables of the high mass analyses in the hadronic channel after the tail cuts as described in sec. 2.1: a) E_γ/E_γ^Z b) $\log(p_T)$ c) log(acollinearity) d) Thrust.

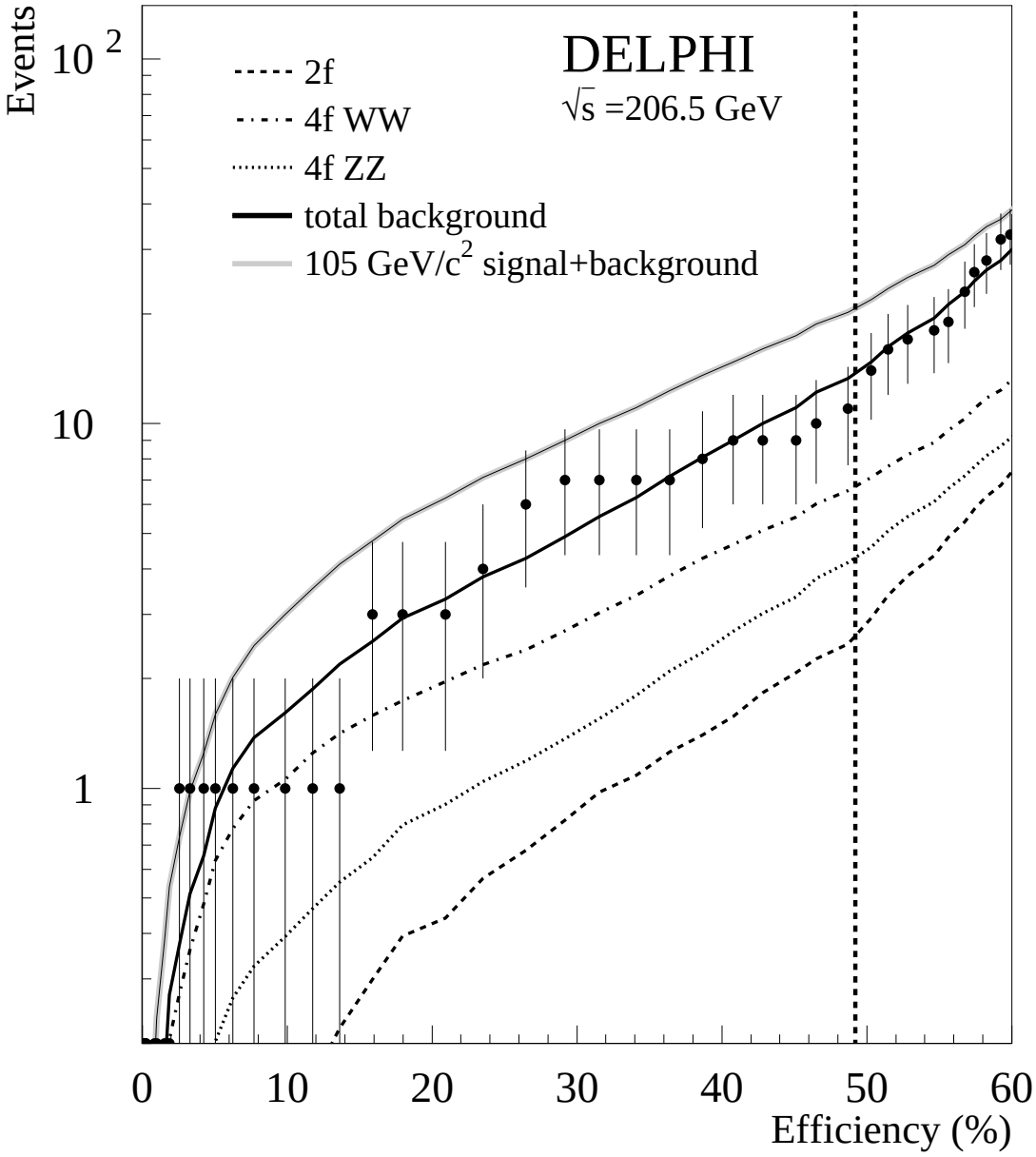

Figure 3: Data and expected background for the 206.5 GeV center-of-mass energy as a function of the efficiency for a Higgs signal of 105 GeV/c^2 in the high-mass hadronic analysis. The indicated lines represent the most important backgrounds with the solid black line showing the sum of all the background processes. In addition the grey line shows the expectation for a 105 GeV/c^2 Higgs signal added on top of the background. The vertical dashed line indicates the working point chosen to maximise the sensitivity.

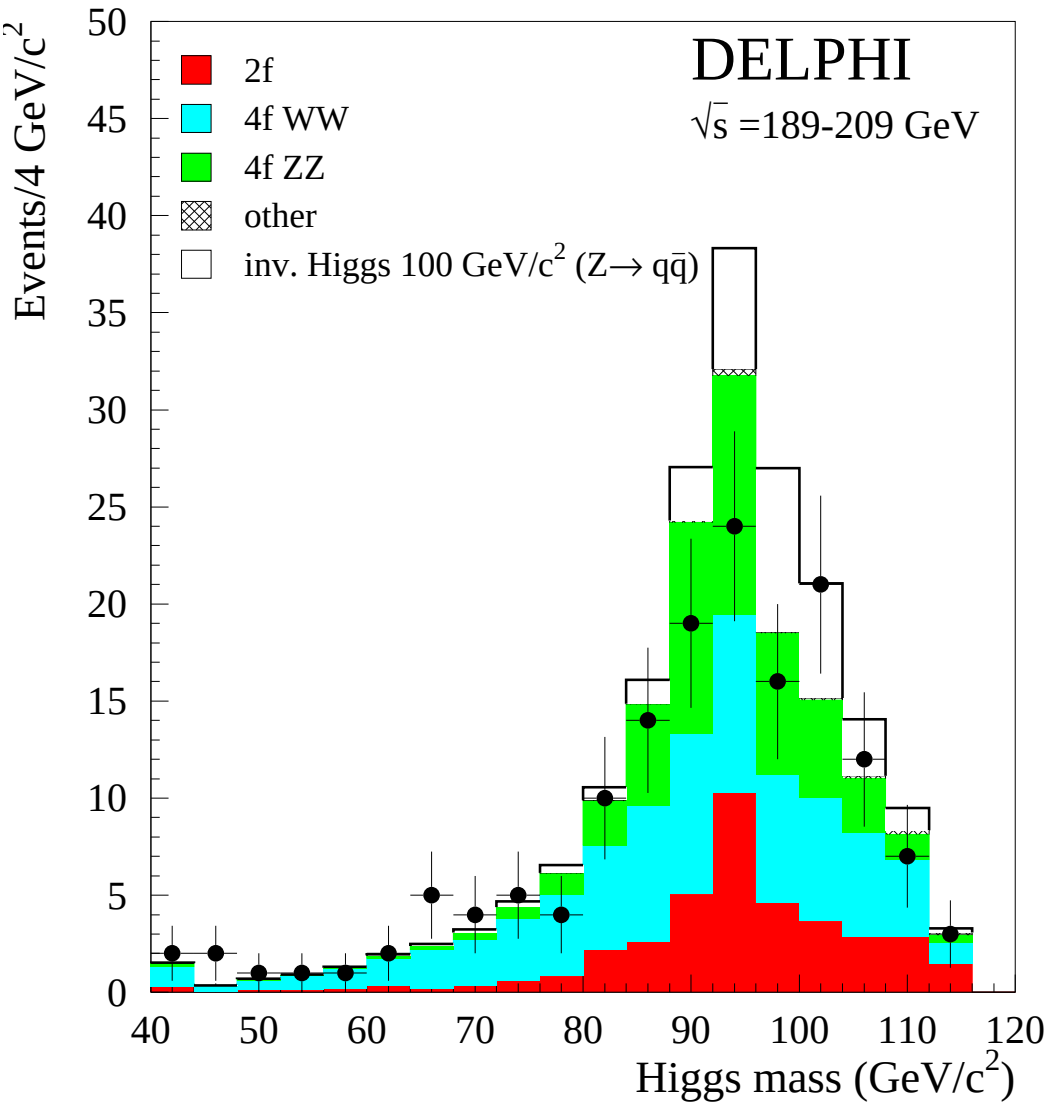

Figure 4: Reconstructed Higgs boson mass for all candidates in the Hq$\bar{\text{q}}$ channel for 189 to 209 GeV after the final selection. Assuming 100% decay into invisible modes.

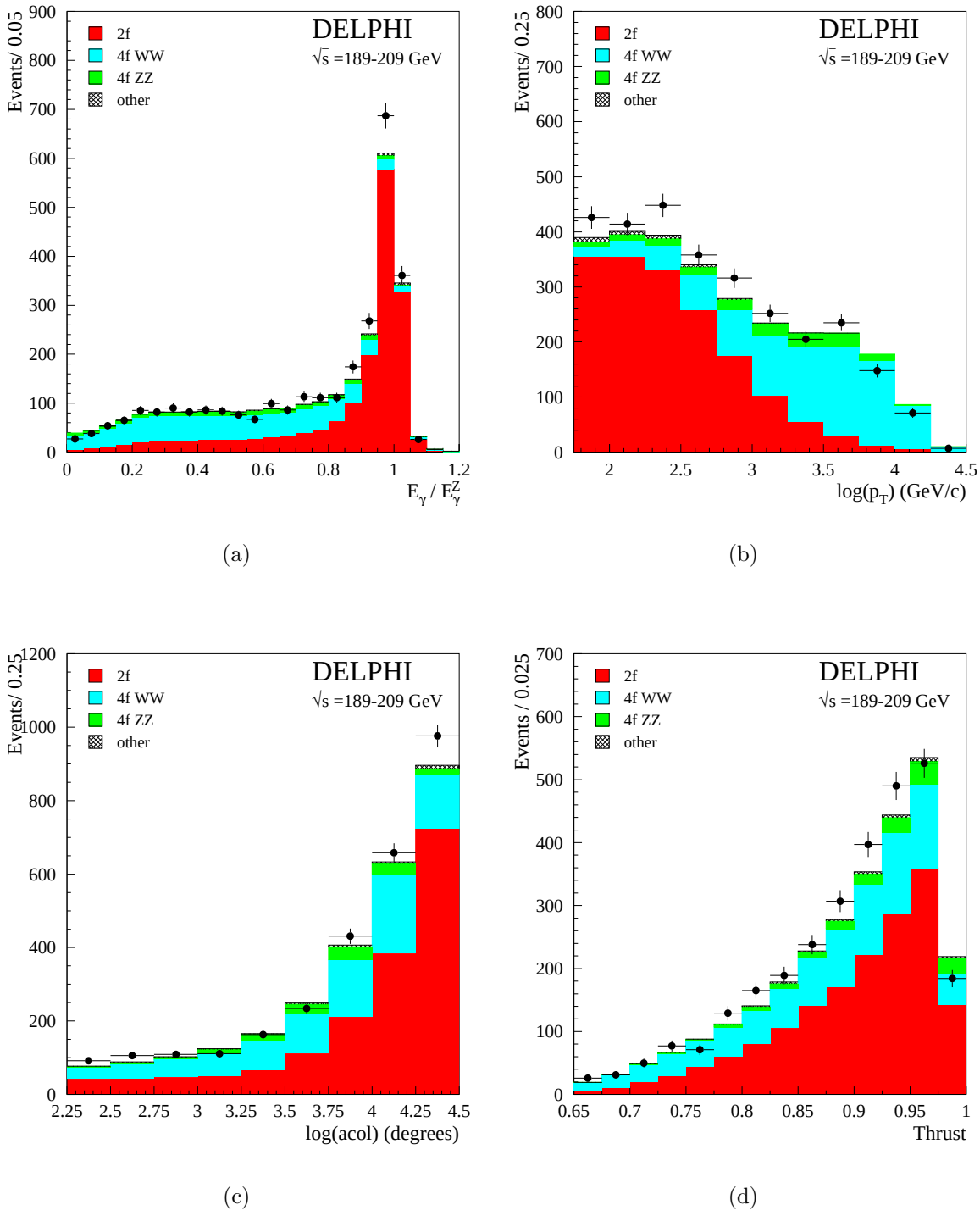

Figure 5: Distributions for the preselection variables of the low mass analyses in the hadronic channel after the tail cuts as described in sec. 2.1: a) E_γ/E_γ^Z b) $\log(p_T)$ c) log(acollinearity) d) Thrust.

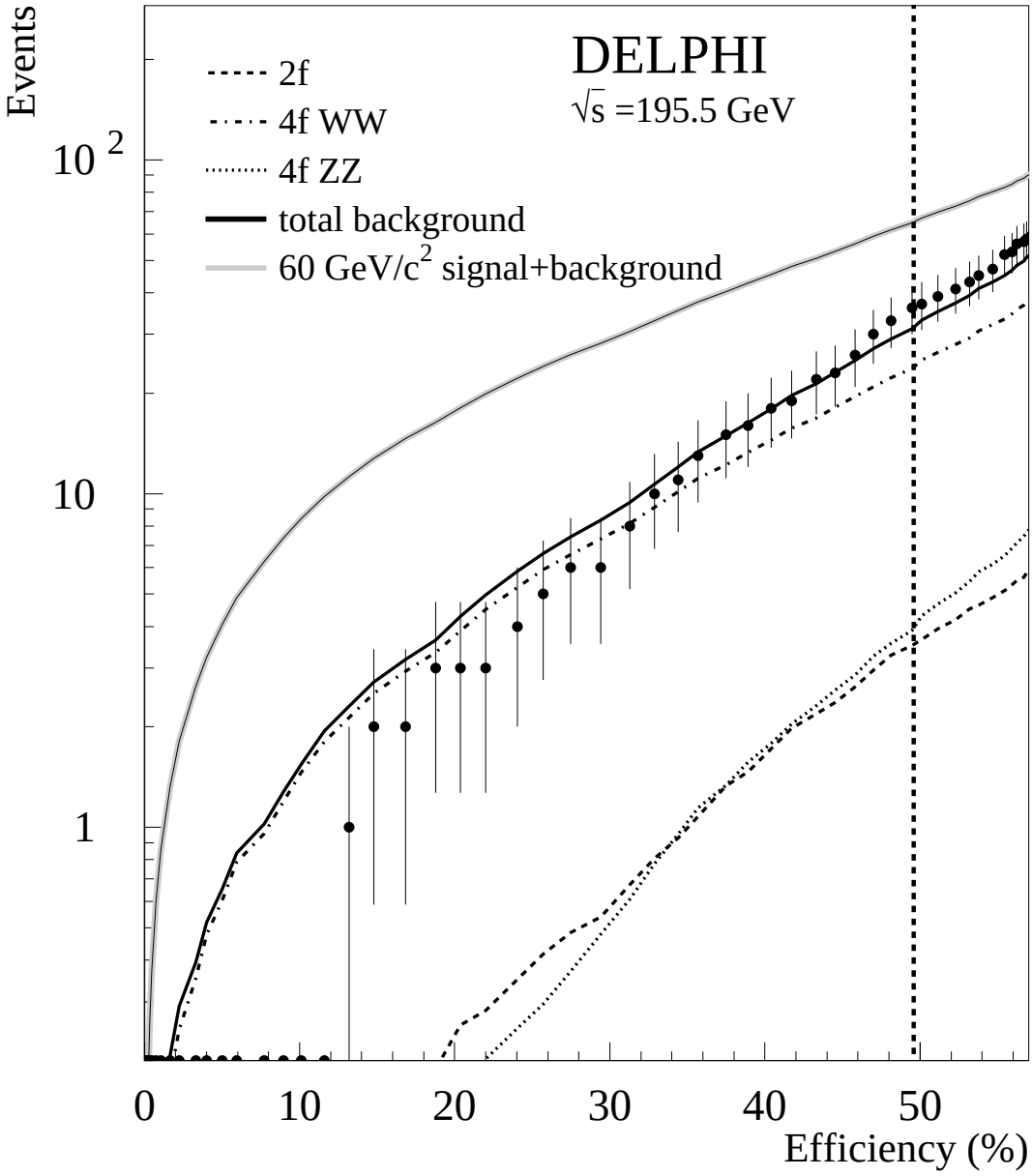

Figure 6: Data and expected background for the 195.5 GeV center-of-mass energy as a function of the efficiency for a Higgs signal of 60 GeV/c^2 in the low-mass hadronic analysis. The indicated lines show number of events from the most important background reactions and the solid black line shows the sum of all the background processes. In addition the grey line shows the expectation for a 60 GeV/c^2 Higgs signal added on top of the background. The vertical dashed line indicates the working point chosen to maximise the sensitivity.

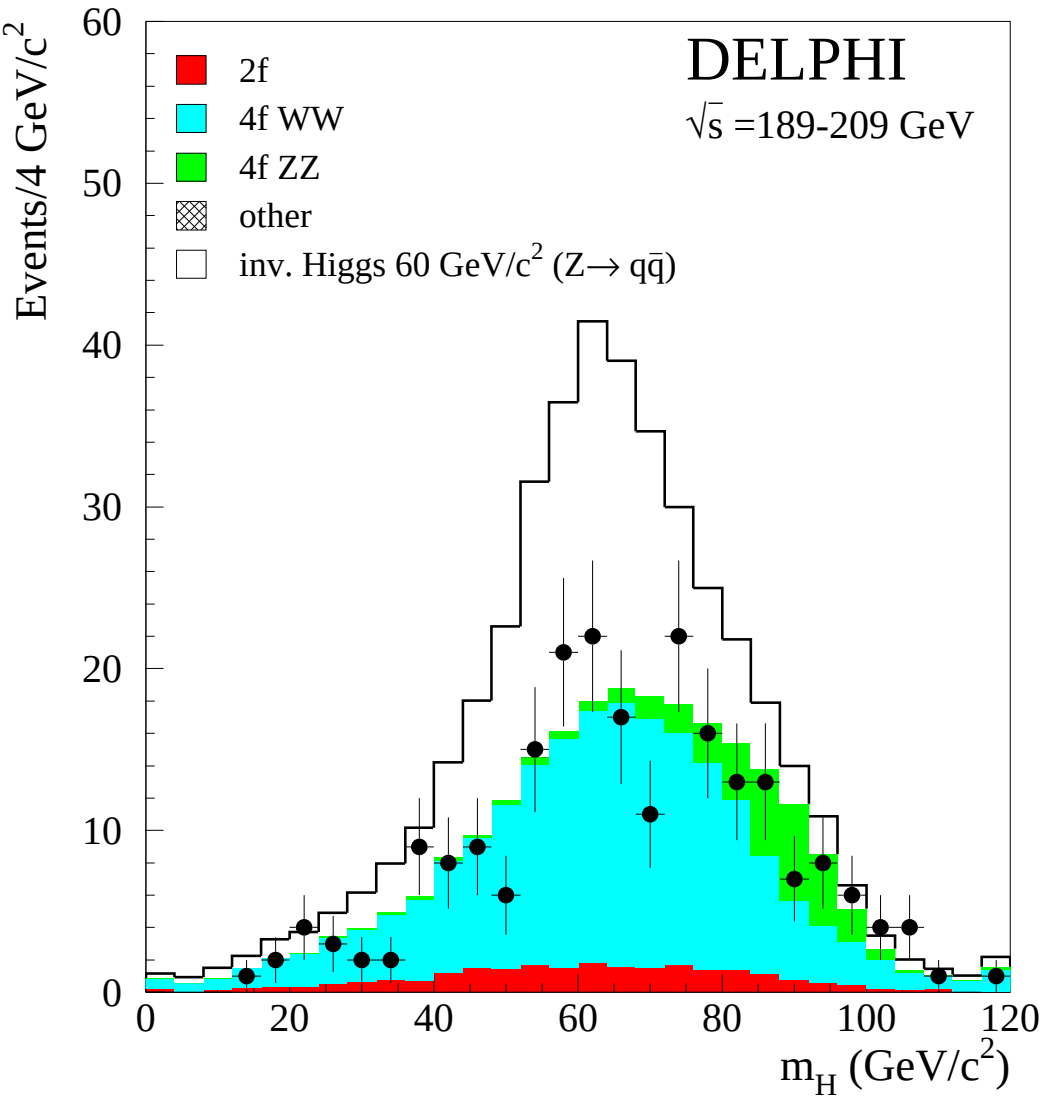

Figure 7: Reconstructed Higgs boson mass for all candidates in the low mass Hq$\bar{\text{q}}$ channel for 189 to 209 GeV after the final selection. Assuming 100% decay into invisible modes.

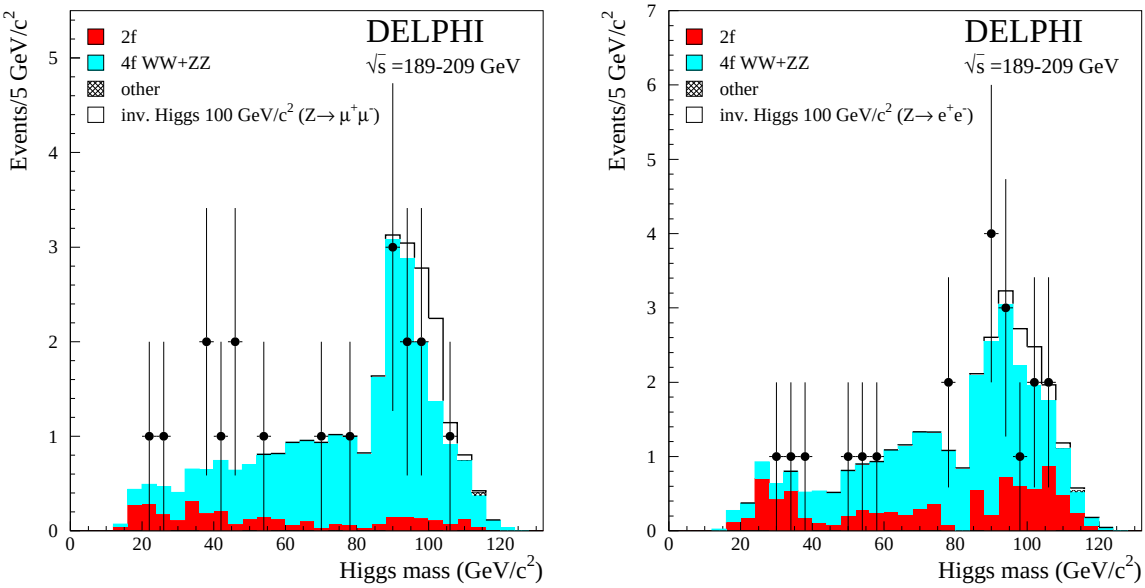

(a)

(b)

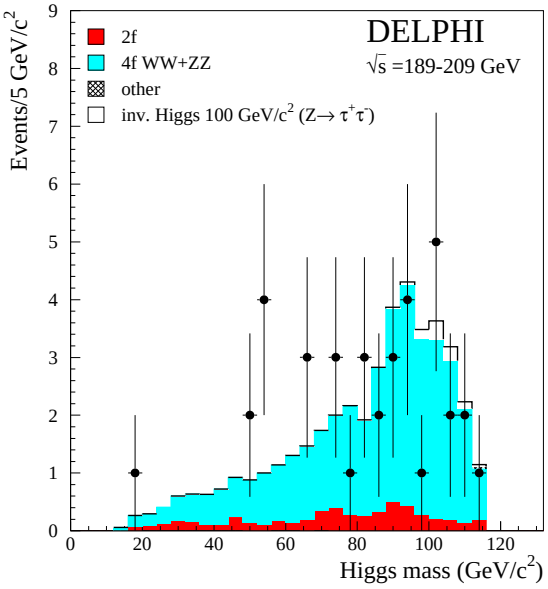

(c)

Figure 8: Reconstructed Higgs boson mass for all candidates in the H$\mu^+\mu^-$channel (a), the He$^+$e$^-$channel (b) and the H$\tau^+\tau^-$channel (c) for 189 to 209 GeV after the final selection.

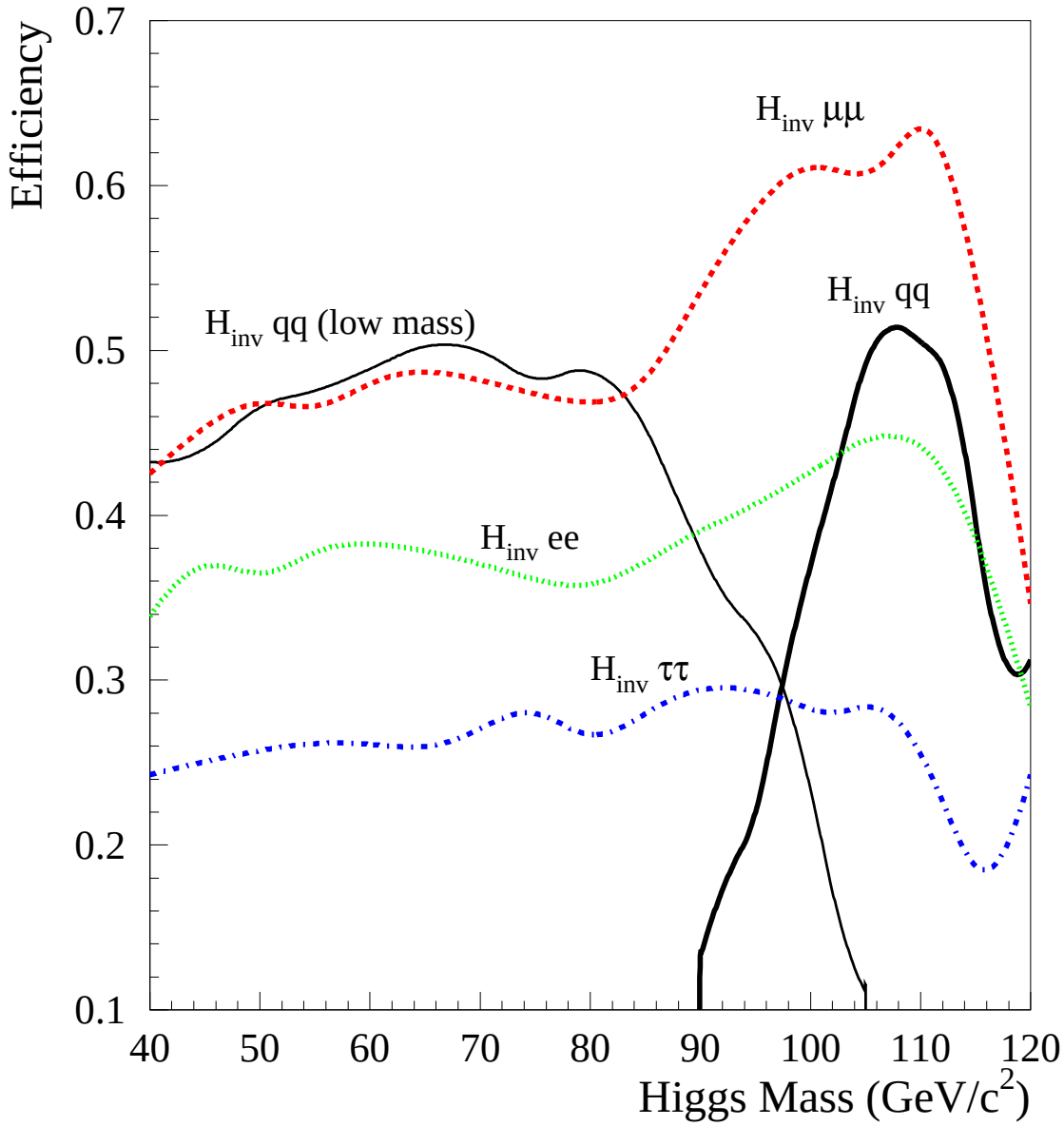

Figure 9: Efficiencies for the Higgs boson masses between 40 and 120 GeV/c^2 for the different selection channels at 206.5 GeV.

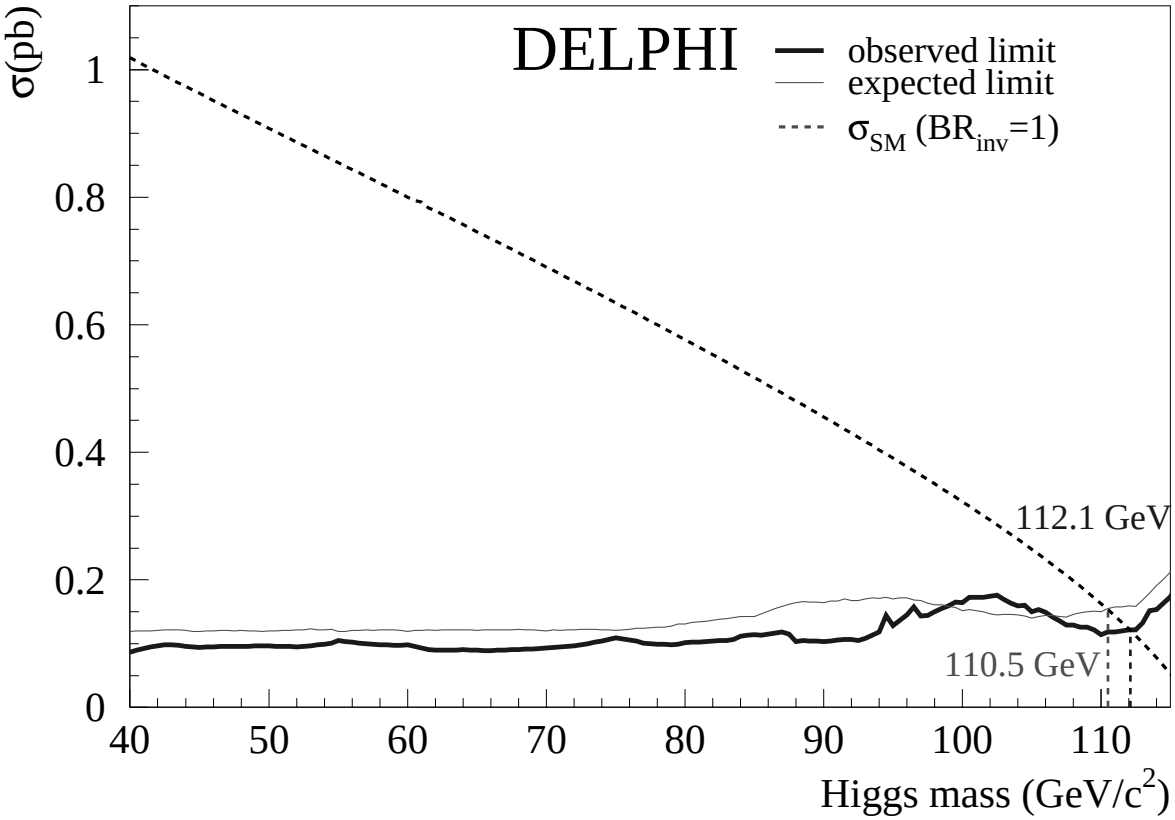

Figure 10: The 95% CL upper limit on the cross-section $e^+e^- \to Z(\text{anything})\,H(\text{invisible})$ as a function of the Higgs boson mass. The dashed line shows the standard model cross-section for the Higgs boson production with $BR_{\text{inv}} = 1$.

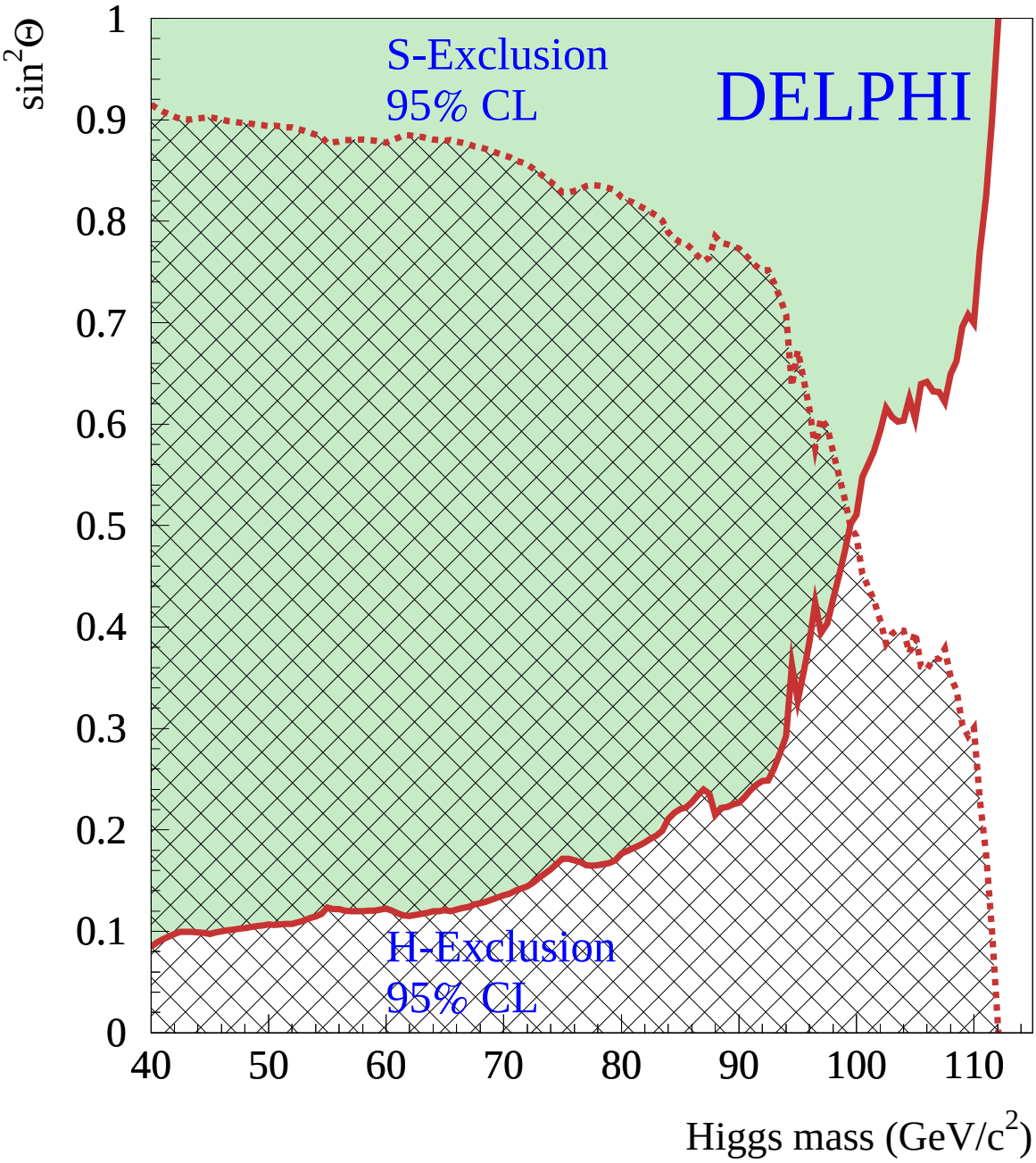

Figure 11: Limit on $\sin^2\theta$ as a function of the Higgs boson mass at 95% CL. S and H are the Higgs bosons in the Majoron model with expected production rates for large $\tan\beta$. In this case the massive Higgs bosons decay almost entirely into invisible Majoron pairs.

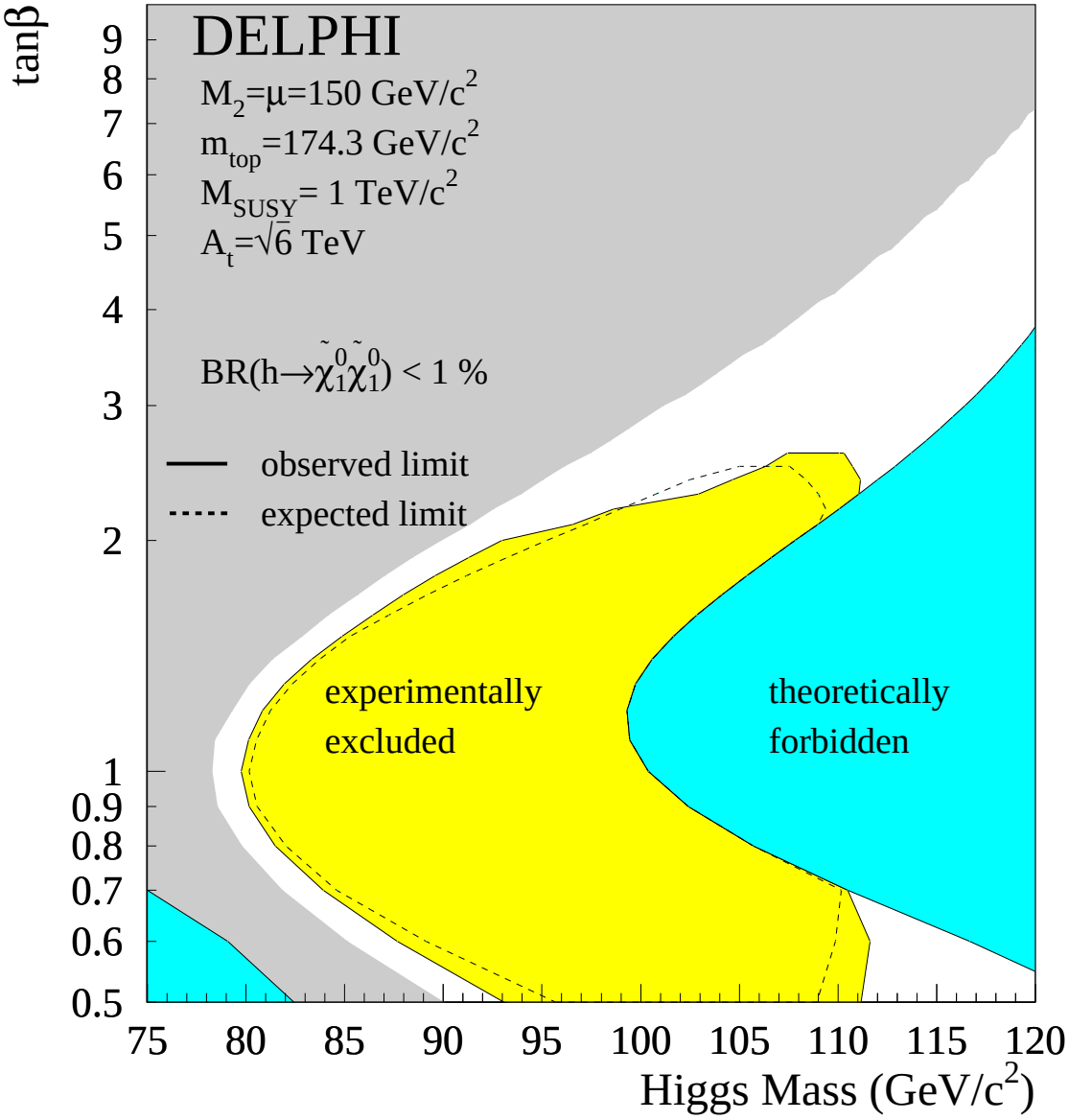

Figure 12: Excluded region in the MSSM from searches for Higgs boson decaying into invisible final states for m_h-max in the stop sector. The different grey areas show the theoretically forbidden region (dark), the region where the Higgs boson does not decay into neutralinos (intermediate), the region which is excluded at 95% CL by this search for invisibly decaying Higgs bosons (light) and the unexcluded region (white).